INTERNATIONAL JOURNAL FOR NUMERICAL METHODS IN FLUIDS
Int. J. Numer. Meth. Fluids **29**: 587–603 (1999)

A DISCONTINUOUS GALERKIN METHOD FOR THE NAVIER–STOKES EQUATIONS

IGOR LOMTEV AND GEORGE EM KARNIADAKIS*,[1]

Division of Applied Mathematics, Center for Fluid Mechanics, Brown University, Providence, RI 02912, USA

SUMMARY

The foundations of a new discontinuous Galerkin method for simulating compressible viscous flows with shocks on standard unstructured grids are presented in this paper. The new method is based on a discontinuous Galerkin formulation *both* for the advective and the diffusive contributions. High-order accuracy is achieved by using a recently developed hierarchical spectral basis. This basis is formed by combining Jacobi polynomials of high-order weights written in a new co-ordinate system. It retains a tensor-product property, and provides accurate numerical quadrature. The formulation is conservative, and monotonicity is enforced by appropriately lowering the basis order and performing h-refinement around discontinuities. Convergence results are shown for analytical two- and three-dimensional solutions of diffusion and Navier–Stokes equations that demonstrate exponential convergence of the new method, even for highly distorted elements. Flow simulations for subsonic, transonic and supersonic flows are also presented that demonstrate discretization flexibility using hp-type refinement. Unlike other high-order methods, the new method uses standard finite volume grids consisting of arbitrary triangulizations and tetrahedrizations. Copyright © 1999 John Wiley & Sons, Ltd.

KEY WORDS: discontinuous Galerkin; spectral methods; compressible flows

1. INTRODUCTION

Despite great research efforts in designing good unstructured grids for aerodynamic flows, especially for three-dimensional simulations, most finite element and finite volume solutions depend strongly on the quality of the grid. In particular, for highly distorted grids, convergence is questionable and in most cases convergence rates are typically less than second-order. Moreover, efforts to increase the accuracy of finite volume methods to higher than second-order have not been very successful as conservativity in the formulation or monotonicity of the solution have to be compromised.

In previous works [1,2], a spectral/hp Galekin method for the numerical solution of the two- and three-dimensional unsteady *incompressible* Navier–Stokes equations on unstructured grids has been developed (parallel code $\mathcal{N}\varepsilon\kappa\mathcal{T}\alpha r$). The discretization is based on arbitrary triangulizations/tesselations of complex geometry domains. On each triangle/tetrahedron, a C^0 spectral expansion basis is employed consisting of Jacobi polynomials of mixed weight that accommodate exact numerical quadrature. The hierarchical expansion basis is of variable

* Correspondence to: Division of Applied Mathematics, Center for Fluid Mechanics, Brown University, Providence, RI 02912, USA. E-mail: gk@cfm.brown.edu
[1] Tel.: +1 401 8631217; fax: +1 401 8633369.

CCC 0271–2091/99/050587–17$17.50

Received July 1997
Revised May 1998

order per element and retains the tensor-product property (similar to standard spectral expansions), which is key in obtaining computational efficiency via the sum factorization technique. The use of a C^0 basis, however, leads to a partial loss of orthogonality, with the resulted global mass and stiffness matrices although sparse not easily invertible.

In this paper, algorithms for the *compressible* Navier–Stokes employing similar high-order spectral/*hp* element discretizations are considered, but following a new formulation that allows the use of orthogonal basis. In particular, a discontinuous Galerkin formulation is developed *both* for the advective as well as the diffusive components of the Navier–Stokes equations. This allows multidomain representation with a discontinuous (i.e. globally L^2) trial basis. This discontinuous basis is orthogonal, hierarchical, and maintains a tensor-product property (even for tetrahedra) [3]. In a previous work [4], a hybrid method based on a discontinuous Galerkin formulation for the hyperbolic contribution and a mixed Galerkin formulation for the diffusive contribution was developed. Such a formulation requires two sets of trial basis, one in L^2 and another one in C^0. The latter trial basis leads to a loss of orthogonality, and thus to a loss of high efficiency, unlike the currently proposed method. Finally, in the proposed formulation, the conservativity property is maintained automatically by the discontinuous Galerkin formulation, while monotonicity is controlled by varying the order of the spectral expansion and by performing *h*-refinement around discontinuities.

The work presented here was motivated by the work of Cockburn and Shu on discontinuous finite elements for hyperbolic problems presented in a series of papers [5–8]. An implementation of these ideas for quadrilateral Legendre spectral elements was developed in [9]. Work on discontinuous Galerkin methods for diffusion is more recent [10], and has been extended to compressible Navier–Stokes equations [11,12]. Discontinuous Galerkin methods use concepts both from finite volume and finite element methodology. In this paper, high-order accuracy is added by using spectral/*hp* expansions on standard unstructured grids. The proposed method is new both in the formulation (e.g. construction of inviscid and viscous fluxes—no need for limiters) as well as in the discretization. It is more efficient than the method developed in [11] as it does not require inversion of the mass matrix, which is diagonal due to the orthogonality of the basis and the exact quadrature. It also presents, for first time, exponential accuracy and flow simulations on three-dimensional unstructured grids.

The paper is organized as follows: in Section 2, the formulation for advection and diffusion scalar equations are presented separately for clarity, and subsequently, the two are combined in the context of compressible Navier–Stokes equations. Also, the new spectral basis on triangles and tetrahedra is reviewed. In Section 3, two- and three-dimensional convergence results are presented, and in Section 4, simulations of subsonic flow past a circular cylinder up to $Re = 10000$, a transonic flow past a NACA0012 airfoil, and a supersonic flow past a NACA4420 airfoil are presented. Section 5 concludes with a brief summary.

2. NUMERICAL FORMULATION

Consider the non-dimensionalized compressible Navier–Stokes equations, which are written in compact form as

$$\vec{U}_t + \nabla \cdot \boldsymbol{F} = Re_\infty^{-1} \nabla \cdot \boldsymbol{F}^v, \tag{1}$$

where $\boldsymbol{F}$ and $\boldsymbol{F}^v$ correspond to inviscid and viscous flux contributions respectively. Here the vector $\vec{U} = [\rho, \rho u, \rho v, \rho w, E]^t$ with (u, v, w) being the local fluid velocity, ρ the fluid density, and E the total internal energy. Splitting the Navier–Stokes operator in this form allows for

a separate treatment of the inviscid and viscous contributions, which in general exhibit different mathematical properties. In the following, the discontinuous Galerkin formulations employed in the proposed method are reviewed briefly. A rigorous analysis of the advection operator was presented in [4], where a mixed formulation was used to treat the diffusion terms. No flux limiters are necessary as has been found in [13] and justified theoretically in [14].

2.1. Discontinuous Galerkin for advection

To explain the formulation, consider the linear two-dimensional equation for advection of a conserved quantity u in a region Ω

$$\frac{\partial u}{\partial t} + \nabla \cdot \boldsymbol{F}(u) = 0, \tag{2}$$

where $\boldsymbol{F}(u) = (f(u), g(u))$ is the *flux* vector that defines the transport of $u(\mathbf{x}, t)$. You start with the variational statement of the standard Galerkin formulation of (2) by multiplying by a test function v and integrating by parts

$$\int_\Omega \frac{\partial u}{\partial t} v \, \mathrm{d}x + \int_{\partial\Omega} v\hat{n} \cdot \boldsymbol{F}(u) \, \mathrm{d}s - \int_\Omega \nabla v \cdot \boldsymbol{F}(u) \, \mathrm{d}x = 0. \tag{3}$$

The solution $u \in \mathscr{X}$ (approximation space) satisfies this equation for all $v \in \mathscr{V}$ (test space). The requirement that $\mathscr{X}$ consist of continuous functions naturally leads to a basis consisting of functions with overlapping support, which implies Equation (3) becomes a banded matrix equation. Solving the corresponding large system is not a trivial task for parallel implementations, and therefore, a different type of formulation is desirable.

Another consideration from the point of view of advection is that continuous function spaces are not the natural place to pose the problem. Mathematically, hyperbolic problems of this type tend to have solutions in spaces of bounded variation. In physical problems, the best one can hope for in practice is that solutions will be piecewise continuous, i.e. be smooth in regions separated by discontinuities (shocks). An additional consideration is that the formulation presented next preserves automatically conservativity in the elementwise sense.

These considerations immediately suggest a formulation where $\mathscr{X}$ may contain discontinuous functions. The discrete space $\mathscr{X}^\delta$ contains polynomials within each 'element', but zero outside the element. Here, the 'element' is, for example, an individual triangular region T_i in the computational mesh applied to the problem. Thus, the computational domain $\Omega = \bigcup_i T_i$, and T_i, T_j overlap only on edges.

Contending with the discontinuities requires a somewhat different approach to the variational formulation. Each element (E) is treated separately, giving a variational statement (after integrating by parts once more):

$$\frac{\partial}{\partial t}(u, v)_\mathrm{E} + \int_{\partial T_\mathrm{E}} v(\tilde{f}(u_\mathrm{i}, u_\mathrm{e}) - \boldsymbol{F}(u_\mathrm{i})) \cdot \mathbf{n} \, ds + (\nabla \cdot \boldsymbol{F}(u), v)_\mathrm{E} = 0, \tag{4}$$

where $\boldsymbol{F}(u_\mathrm{i})$ is the flux of the interior values. Computations on each element are performed separately, and the connection between elements is a result of the way boundary conditions are applied. Here, boundary conditions are enforced via the numerical surface flux $\tilde{f}(u_\mathrm{i}, u_\mathrm{e})$ that appears in Equation (4). Because this value is computed at the boundary between adjacent elements, it may be computed from the value of u given at either element. These two possible values are denoted here as u_i in the interior of the element under consideration and u_e in the exterior (see Figure 1). Upwinding considerations dictate how this flux is computed. In the

more complicated case of a hyperbolic system of equations, an approximate Riemann solver should be used to compute a value of f, g, h (in three dimensions) based on u_i and u_e.

Specifically, the flux $\tilde{f}(u_i, u_e)$ is computed using upwinding, i.e.

$$\tilde{f}(u) = R\Lambda^+ Lu_i + R\Lambda^- Lu_e,$$

where A (the Jacobian matrix of $\boldsymbol{F}$) is written in terms of the left and right eigenvectors, i.e. $A = R\Lambda L$, with Λ containing the corresponding eigenvalues in the diagonal; also, $\Lambda^{\pm} = (\Lambda \pm |\Lambda|)/2$. Alternatively, a standard Roe-splitting flux can be used

$$\tilde{f}(u) = \frac{1}{2}(f(u_e) + f(u_i)) - \frac{1}{2} R|\Lambda|L(u_e - u_i).$$

This last form is what is used in the examples presented here.

2.2. Discontinuous Galerkin for diffusion

Consider as a model problem, the parabolic equation with variable coefficient v to demonstrate the treatment of the viscous contributions:

$$u_t = \nabla\cdot(v\nabla u) + f \quad \text{in } \Omega, \quad u \in L^2(\Omega),$$

$$u = g(\mathbf{x}, t) \quad \text{on } \partial\Omega.$$

Then the flux variable is introduced

$$\mathbf{q} = -v\nabla u,$$

with $\mathbf{q}(\mathbf{x}, t) \in \mathbf{L}^2(\Omega)$, and rewrite the parabolic equation

$$u_t = -\nabla\cdot\mathbf{q} + f, \quad \text{in } \Omega,$$

$$1/v\mathbf{q} = -\nabla u, \quad \text{in } \Omega,$$

$$u = g(\mathbf{x}, t), \quad \text{on } \partial\Omega.$$

The weak formulation of the problem is then:
Find $(\mathbf{q}, u) \in \mathbf{L}^2(\Omega) \times L^2(\Omega)$ such that

$$(u_t, w)_E = (\mathbf{q}, \nabla w)_E - \langle w, \mathbf{q}_b\cdot\mathbf{n}\rangle_E + (f, w)_E, \quad \forall w \in L^2(\Omega),$$

$$1/v(\mathbf{q}^m, \mathbf{v})_E = (u, \nabla\cdot\mathbf{v})_E - \langle u_b, \mathbf{v}\cdot\mathbf{n}\rangle_E, \quad \forall \mathbf{v} \in \mathbf{L}^2(\Omega),$$

$$u = g(\mathbf{x}, t), \quad \text{on } \partial\Omega,$$

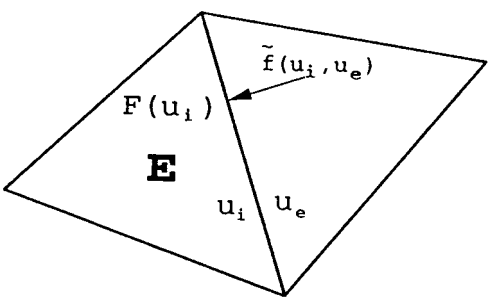

Figure 1. Interface conditions between two adjacent triangles.

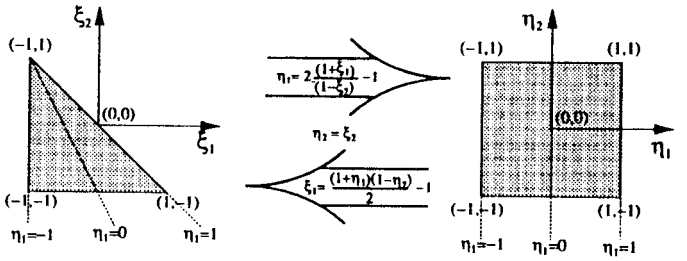

Figure 2. Triangle-to-rectangle transformation.

where the parentheses denote standard inner product in an element (E) and the angle brackets denote boundary terms on each element, with **n** denoting the unit outwards normal. The surface terms contain weighted boundary values of v_b, q_b, which can be chosen as the arithmetic mean of values from the two sides of the boundary, i.e. $v_b = 0.5(v_i + v_e)$ and $q_b = 0.5(q_i + q_e)$.

By integrating by parts once more, you obtain an equivalent formulation which is easier to implement and it is actually used in the computer code. The new variational problem is

$$(u_t, w)_E = (-\nabla\cdot\mathbf{q}, w)_E - \langle w, (\mathbf{q}_b - \mathbf{q}_i)\cdot\mathbf{n}\rangle_E + (f, w)_E, \quad \forall w \in L^2(\Omega),$$

$$1/v(\mathbf{q}, \mathbf{v})_E = (-\nabla u, \mathbf{v})_E - \langle u_b - u_i, \mathbf{v}\cdot\mathbf{n}\rangle_E, \quad \forall \mathbf{v} \in \mathbf{L}^2(\Omega),$$

$$u = g(\mathbf{x}, t), \quad \text{in } \partial\Omega,$$

where the subscript i denotes contributions evaluated at the interior side of the boundary.

2.3. Spectral/hp element discretization

This subsection begins with a definition of a convenient set of local co-ordinates upon which the expansions can be constructed. Moving away from the use of barycentric co-ordinates, which are typically applied to unstructured domains, a set of *collapsed Cartesian* co-ordinates in non-rectangular domains is defined. These co-ordinates will form the foundation of the polynomial expansions. The new co-ordinate system is based upon the transformation of a triangular region to a rectangular domain (and *vice versa*), as shown in Figure 2. The main effect of the transformation is to map the vertical lines in the rectangular domain (i.e. lines of constant η_1) onto lines radiating out of the point ($\xi_1 = -1$, $\xi_2 = 1$) in the triangular domain. The triangular region can now be described using the 'ray' co-ordinate (η_1) and the standard horizontal co-ordinate ($\xi_2 = \eta_2$). The triangular domain is therefore defined by ($-1 \le \eta_1, \eta_2 \le 1$) rather than the Cartesian description ($-1 \le \xi_1, \xi_2;\ \xi_1 + \xi_2 \le 0$), where the upper bound couples the two co-ordinates. As illustrated in Figure 3, the same transformation can be repeatedly applied to generate a new co-ordinate system for the tetrahedron.

A polynomial expansion for the tetrahedron can be developed based upon the new local co-ordinate system. This expansion can be expressed as polynomials in terms of the local co-ordinates as well as the Cartesian co-ordinates (ξ_1, ξ_2, ξ_3). This is a significant property as primary operations, such as integration and differentiation, can be performed with respect to the local co-ordinates, but the expansion may still be considered as a polynomial expansion in terms of the Cartesian system.

Expansions that are orthogonal in the Legendre inner product are considered. Three principle functions $\phi_i^a(z)$, $\phi_{ij}^b(z)$ and $\phi_{ijk}^c(z)$, are defined in terms of the Jacobi polynomial, $P_p^{\alpha,\beta}(z)$, as:

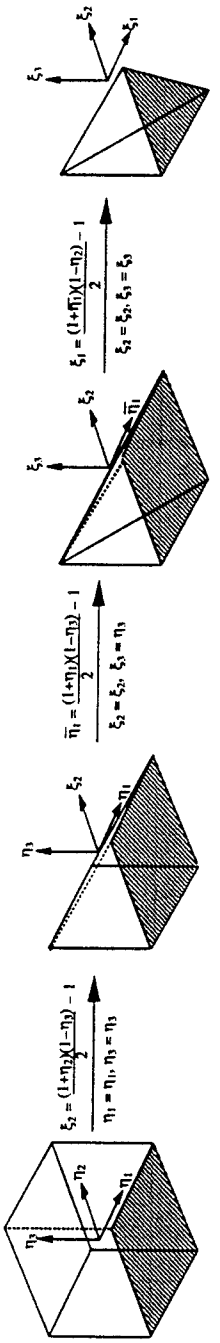

Figure 3. Hexahedron-to-tetrahedron transformation.

$$\phi_i^{\mathrm{a}}(z) = P_i^{0,0}(z), \qquad \phi_{ij}^{\mathrm{b}}(z) = \left(\frac{1-z}{2}\right)^i P_j^{2i+1,0}(z), \qquad \phi_{ijk}^{\mathrm{c}}(z) = \left(\frac{1-z}{2}\right)^{i+j} P_k^{2i+2j+2,0}(z).$$

Using these functions, an orthogonal polynomial expansion on a tetrahedron can be constructed:

$$\phi_{pqr}(\xi_1, \xi_2, \xi_3) = \phi_p^{\mathrm{a}}(\eta_1)\phi_{pq}^{\mathrm{b}}(\eta_2)\phi_{pqr}^{\mathrm{c}}(\eta_3),$$

where

$$\eta_1 = \frac{2(1+\xi_1)}{(-\xi_2-\xi_3)} - 1, \qquad \eta_2 = \frac{2(1+\xi_2)}{(1-\xi_3)} - 1, \qquad \eta_3 = \xi_3,$$

are the local co-ordinates. In the following, the maximum polynomial order will be denoted as P, and this can be varying from one element to another.

An important property of this tetrahedral spectral basis is that it is orthogonal in the new co-ordinate system that is introduced; unlike the expansions developed in [2]. This is possible as the C^0 continuity condition of the basis in the discontinuous Galerkin formulation is not required. This greatly simplifies the formulation since all mass matrices are diagonal and their inversion is trivial. Finally, it is noted that the bases are all *hierarchical*, which means that increasing the polynomial order of any expansion simply adds extra modes to the existing basis. Hierarchical expansions naturally lead to p-type adaptivity, where the polynomial order of the expansion can differ within each elemental domain. This is a very attractive property as it permits the polynomial order of the expansion to be altered in order to capture the spatial characteristics of the solution.

3. CONVERGENCE

This section demonstrates the exponential convergence of the discontinuous Galerkin method, first for the parabolic equation and second for the compressible Navier–Stokes equations.

The first benchmark problem is for a curved 2D geometry as shown Figure 4. An analytical solution of the parabolic equation $u_t = \nabla^2 u$ of the form

$$u = \mathrm{e}^{-2t} \sin x \sin y$$

is employed with corresponding Dirichlet boundary conditions. Exponential convergence of the method is shown in Figure 4, where the results from a discretization using a mixed formulation [4] are included. The accuracy of the mixed method is slightly better, because the flux variable $\mathbf{q}$ is computed (for stability) in the space of polynomials of one degree higher than the original function u, unlike the discontinuous Galerkin formulation. Here, the big computational gain offered by using the discontinuous Galerkin formulation should be mentioned. Since the basis for this formulation is orthogonal, the matrix is diagonal and thus trivial to invert. In contrast, in the mixed Galerkin formulation, since $\mathbf{q}$ is continuous, a global mass matrix has to be inverted at every time step, which makes the computation more expensive. The error plot in Figure 4 shows P-convergence. Figure 5 also examines h-convergence. The polynomial order was fixed in each element and the number of elements was varied from 16 to 1024. Four different geometries of with $n_{\mathrm{el}} = 16$, 256, 512 and 1024 elements in a square domain were considered. The plot shows accuracy of order $\mathcal{O}(h^{P+1})$ (for even P) and (*at least*) of order $\mathcal{O}(h^P)$ (for odd P), in agreement with the 1D results and theory of [10].

The next test demonstrates how convergence is affected by element distortion. The parabolic equation $u_t = \nabla^2 u$ is solved for an analytical solution of the form

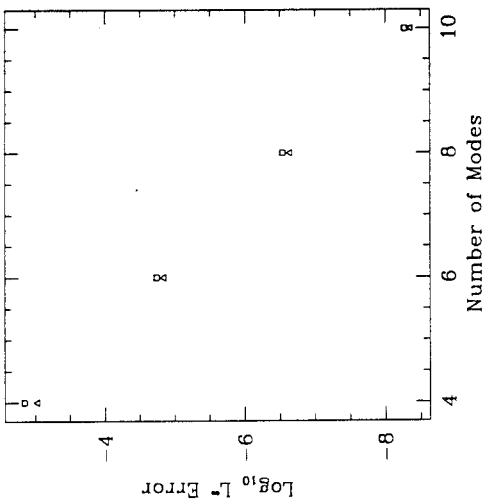

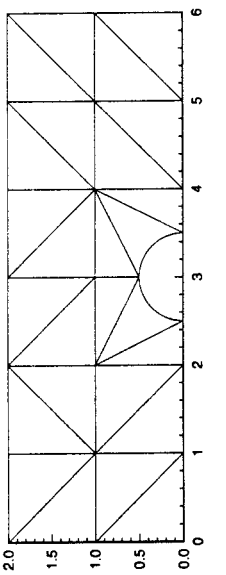

Figure 4. Parabolic equation: /Computational domain (left) and error plot (right). △ corresponds to mixed Galerkin method, □, discontinuous Galerkin method.

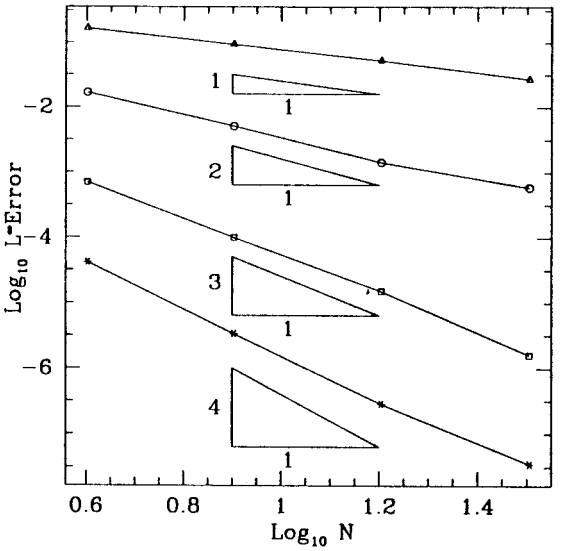

Figure 5. L_∞ error of a parabolic problem as a function of the number of elements. △, 0th polynomial order (constants); ○, 1st order; □, 2nd order; ∗, 3rd order. L_∞ and the number of elements are in logarithmic scale.

$$u = e^{\pi^2 t/12} \sin\frac{\pi x}{6} \sin\frac{\pi y}{6} \sin\frac{\pi z}{6},$$

with exact boundary conditions prescribed at all boundaries. The integration is for 1000 time steps with $\Delta t = 10^{-5}$ to eliminate any temporal errors. Four different meshes consisting of 12 tetrahedra, as shown in Figure 6, are considered. All tetrahedra share a common vertex at the center of the box, which is moved as shown to cause distortion of the tetrahedra. In the

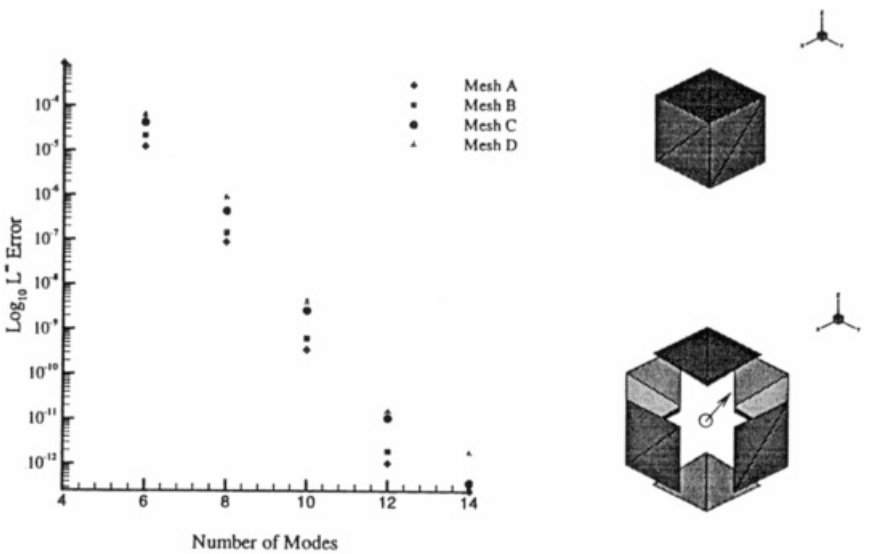

Figure 6. L_∞ error of a 3D parabolic problem as a function of the number of modes. Domain D has elements with aspect ratio of 20.

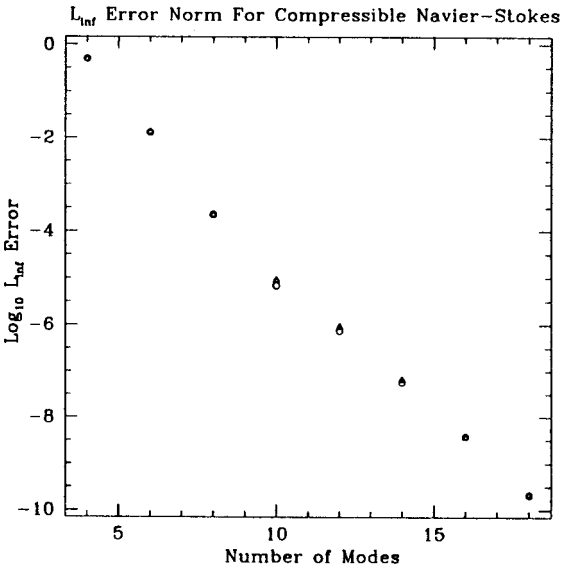

Figure 7. L_∞ error vs. the expansion order for the energy of an analytic solution of the steady 2D Navier–Stokes equations obtained by (1) $\triangle$, discontinuous; (2) $\bigcirc$, mixed Galerkin formulation.

domain D, elements with aspect ratio of 20 are obtained. The error plot of Figure 6 shows that there is a small effect of distortion, but exponential convergence is maintained.

To test the accuracy of the Navier–Stokes algorithm, analytical solutions are used. First, two dimensions on a square domain, defined by the left-low and right-up corners ($[-1, -1]$, $[1, 1]$) and discretized in eight triangles, are considered. On the left and right sides, periodic boundary conditions are assumed and on the top and bottom Dirichlet boundary conditions are prescribed. The analytical solution has the form

$$\rho = A + B\sin(\omega x), \qquad u = C + D\cos(\omega x)\sin(\omega y), \qquad T = E + Fy,$$

where $\omega = \pi$, $A = 1$, $B = 0.1$, $C = 1$, $D = 0.04$, $E = 84$ and $F = 28$. The Navier–Stokes equations are then integrated using a forcing term consistent with the above solution. Figure 7 shows the comparison of the L_∞ error for the total energy, where the viscous part was computed using mixed (see [4]) and discontinuous Galerkin formulations. The results are almost identical and show exponential convergence.

Next, the convergence of the method in a three-dimensional domain, as shown in Figure 8, is tested numerically. The analytical solution has the form

$$\rho = A + B\sin(\omega x), \qquad u = C + D\cos(\omega x)\sin(\omega y)\cos(\omega z), \qquad T = E + Fy + Gz^2,$$

where $\omega = \pi/2$, $A = 1$, $B = 0.1$, $C = 1$, $D = 0.04$, $E = 84$, $F = 28$ and $G = 10$. Exponential convergence is demonstrated in Figure 8.

4. SIMULATIONS

Next, subsonic and supersonic flow simulations are presented. Firstly, a subsonic flow past a circular cylinder performed on the domain shown in Figure 9 is compared with the trianguliza-

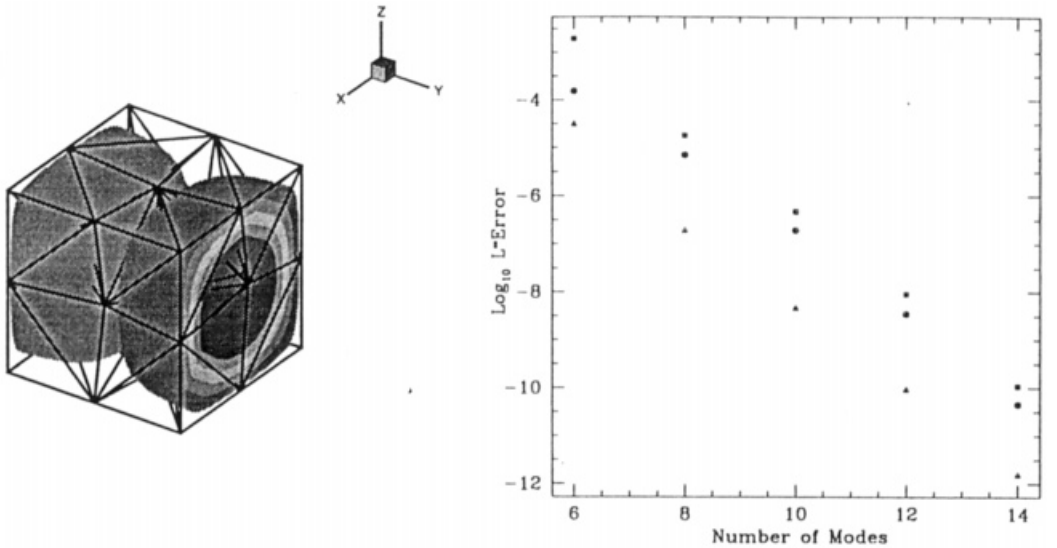

Figure 8. L_∞ error vs. the expansion order for the energy (■), momentum (●) and density (▲) of an analytic solution of the steady 3D Navier–Stokes equations.

tion; 462 elements were used and two sets of simulations were performed, one at order $P = 4$ and one at order $P = 6$. In Figure 10 shows density contours and streamlines of the instantaneous field that shows the von Karman vortex street observed in low Mach number flows.

In Figure 10, the centerline average velocity versus the streamwise distance is plotted for both the low and high resolution as well as for another simulation based on a spectral element (collocation) formulation for subsonic flows [15]. Also, the current results are compared with

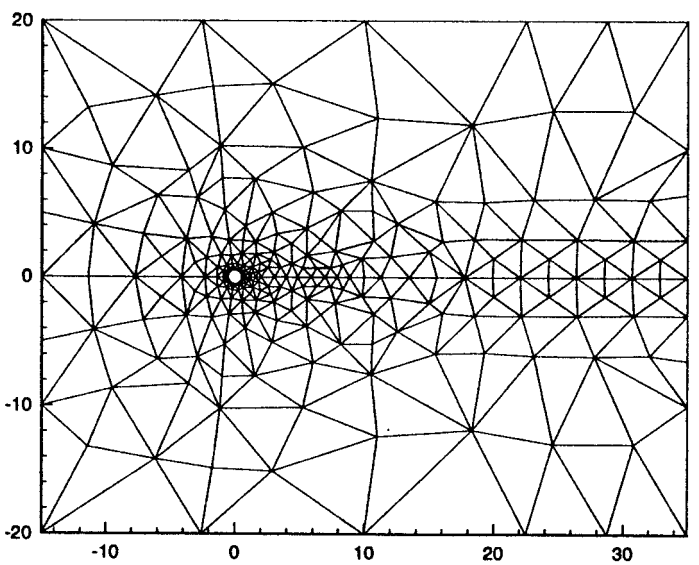

Figure 9. Computational domain for subsonic flow past a cylinder; 462 elements are used in the discretization.

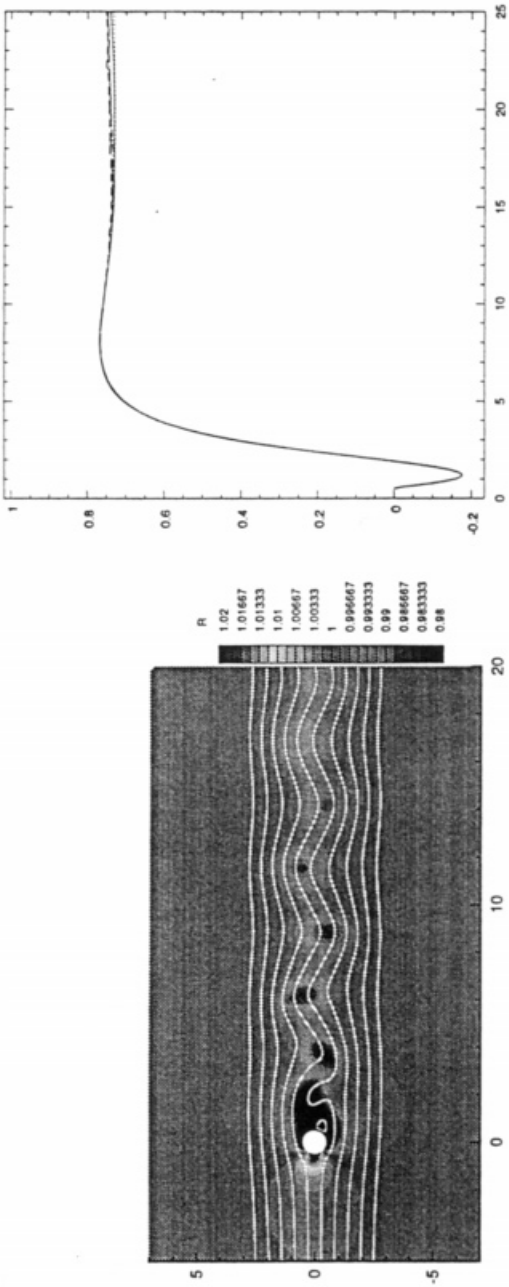

Figure 10. Left: instantaneous density contours and streamlines for flow past a circular cylinder at Mach number 0.2 and Reynolds number 100. Right: average centerline velocity. Shown with solid line is the high resolution simulation ($P = 6$), with dash line the low resolution simulation ($P = 4$), and with dot line simulation using a spectral element collocation scheme due to Beskok [15].

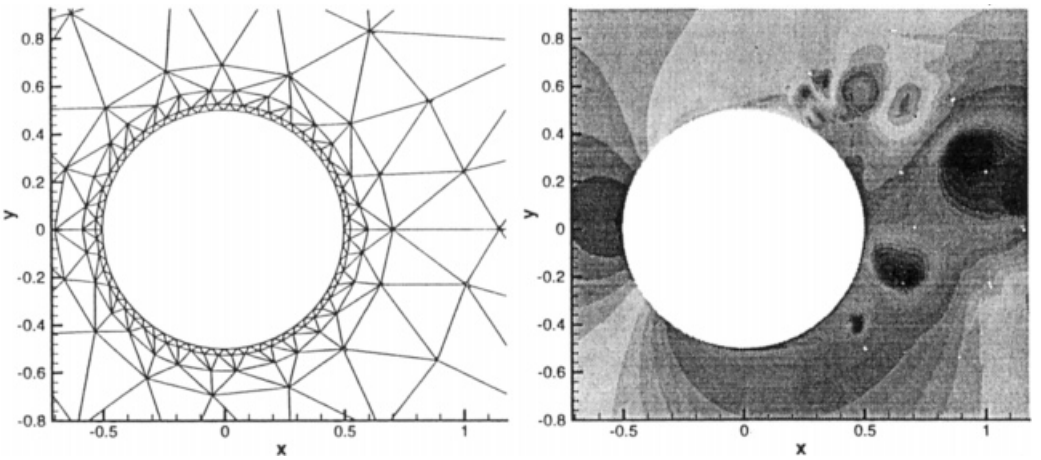

Figure 11. Left: discretization around a cylinder; 680 elements are used. right: instantaneous density contours at Mach number 0.2 and Reynolds number 10000.

results obtained with a code using a mixed formulation for the viscous terms [4]. The Strouhal number (non-dimensional frequency) is 0.1659 (mixed formulation: 0.1656), which is in agreement with the experimental results reported in [16]. The drag coefficient is 1.3764 (mixed formulation: 1.3757), which is in good agreement with a simulation of corresponding incompressible flow [17] and with the experimental value 1.35. Also, the lift coefficient is 0.339 (mixed formulation: 0.333), again in good agreement with the simulations in [17].

The flexibility in discretization is demonstrated in Figure 11, showing the grid used when the Reynolds number was increased to $Re = 10000$. A similar mesh of large elements is used, except around the cylinder where an h-refinement is performed. Elements of variable polynomial order are then used away from the cylinder. The total number of elements is $n_{el} = 680$ and the maximum order used is $P = 6$. An instantaneous plot of the density in the near-wake is also shown in Figure 11, which clearly shows the shear layer instability observed experimentally

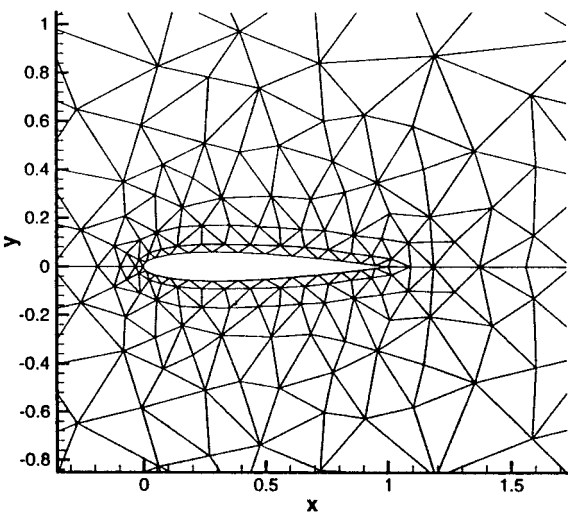

Figure 12. Discretization around a NACA0012 airfoil; 592 elements are used.

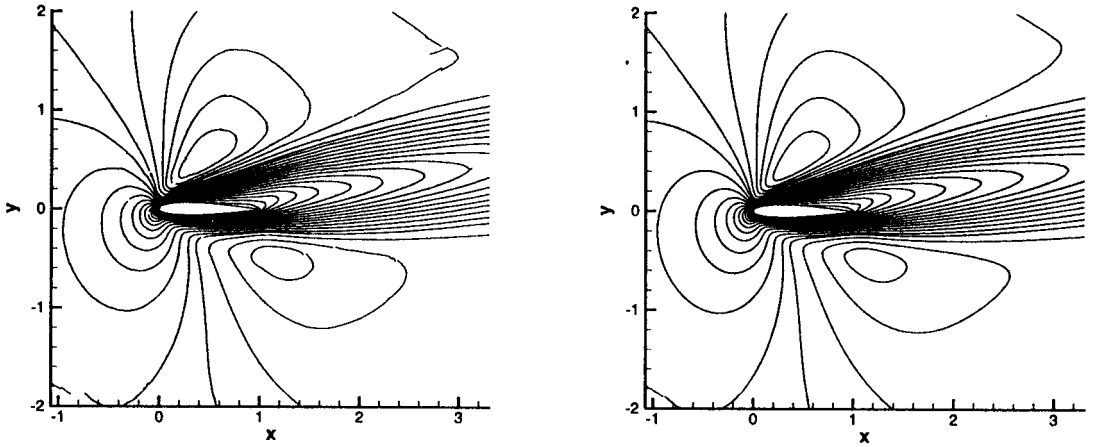

Figure 13. Mach contour lines for discretization with $P = 2$ (left) and $P = 4$ (right).

[18]. The Strouhal frequency is $St = 0.2446$, higher than the experimental value as expected for this 2D simulation.

Considered next is a refinement study for a transonic flow past an airfoil NACA0012 at an angle of attack $\alpha = 10°$, free-stream Mach number $Ma = 0.8$, and Reynolds number based on the free-stream velocity and the airfoil chord equal to $Re = 73$. The wall temperature is equal to the free-stream total temperature. The same problem is considered in [11] and is one of the benchmark problems suggested in the GAMM (1986) workshop [19]. The mesh is shown in Figure 12; it extends four chords downstream and consists of 592 elements, which is about a quarter of the number used in [11]. Three different discretizations with P-refinement were used, corresponding to order 2, 4 and 6. The maximum order used in [11] was 3. In Figure 13, Mach contours are plotted for the first two discretizations ($P = 2$ and 4) that show the improvement in the solution as the polynomial order is increased. A more quantitative comparison is shown in Table I, where the drag and lift coefficients for the three meshes are presented; very good agreement with the results of [11] is obtained. The same is true for the distribution of the pressure and friction coefficients around the airfoil, as shown in Figure 14.

The last simulation is a supersonic flow past a NACA 4420 airfoil at Mach number 2 and Reynolds number (based on the chord length) 2400; the angle of attack is 20°. The domain extends from 1.25 chords upstream to 3.75 chords downstream and is discretized with 1492 triangles. Discretization and density contours and streamlines are shown in Figure 15; the results are identical to earlier results obtained with results using a mixed formulation in [4]. Variable polynomial order is used from zero (constant elements) around the shock to $P = 5$ in the wake. No flux limiters or filtering were used in this simulation.

Table I. Drag and lift coefficients corresponding to different P-refinements

Item	$P = 2$	$P = 4$	$P = 6$
C_d	0.68287	0.67858	0.6758
C_l	0.47625	0.53022	0.53173

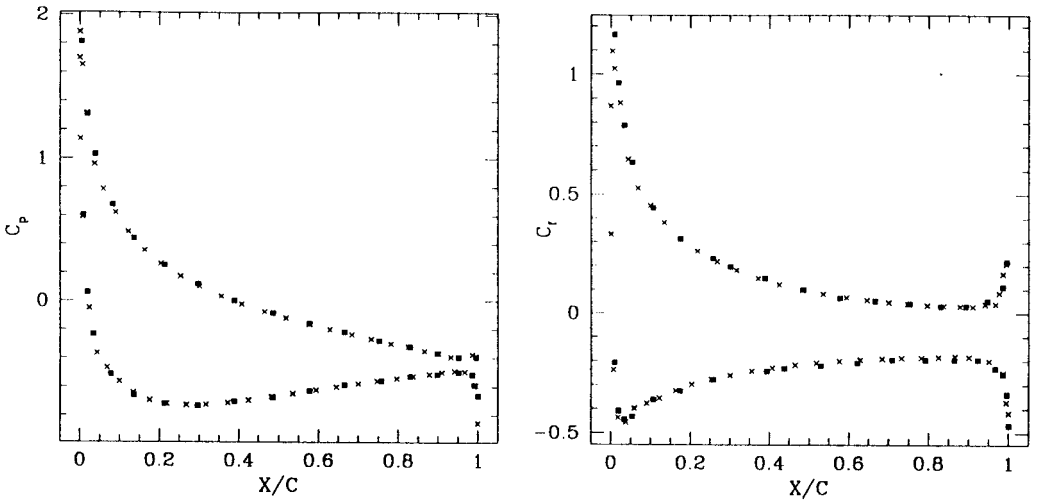

Figure 14. Pressure (left) and drag (right) coefficients; ■, data from [11] and ×, from the current simulation for $P = 6$.

5. SUMMARY

We have developed a new method for solving compressible Navier–Stokes equations on standard unstructured grids consisting of arbitrary triangles and tetrahedra, and presented several convergence tests and flow simulations for validation. The new method is based on a discontinuous Galerkin treatment of the advective and diffusive component. This, in turn, allows the use of orthogonal tensor-product spectral basis in these non-orthogonal subdomains, which results in high computational efficiency. In particular, the computational cost is $n_{\text{el}} = P^{d+1}$ (where $d = 2$ or 3 in 2D and 3D respectively) with n_{el} being the number of elements and P the polynomial order in an element. This cost corresponds to the differentiation and

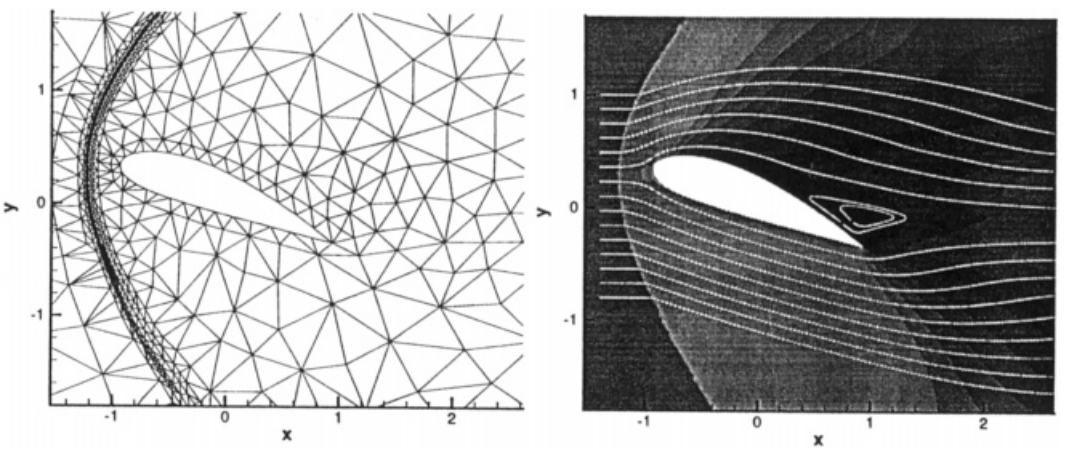

Figure 15. Discretization around a NACA4420 airfoil (left) and density contours and streamlines (right); Mach number 2.

integration costs on the entire domain and is similar to the cost of such operations in standard global methods in simple separable domains [20]. The only matrix inversion required is that of a *local* mass matrix, which is diagonal, and thus trivial to invert.

Spectral and high-order methods in solving compressible viscous flows in the presence of shocks have not been popular in the past due primarily to problems associated with solution monotonicity. Typically, filtering, limiters or non-oscillatory reconstruction algorithms are involved, which are neither efficient nor robust for most aerodynamic applications (see [21,22]). The method presented here borrows from features of finite volumes, finite elements and spectral methods, and is both robust and flexible as it is conservative, it does not rely on flux limiters, and it works on standard unstructured grids.

ACKNOWLEDGMENTS

The authors would like to thank Professor C.-W. Shu, Dr C.B. Quillen, Dr S.J. Sherwin and Mr T.C. Warburton for many useful suggestions regarding this work. This work was supported by AFOSR.

REFERENCES

1. S.J. Sherwin and G.E. Karniadakis, 'A triangular spectral element method; applications to the incompressible Navier–Stokes equations', *Comp. Methods Appl. Mech. Eng.*, **23**, 83 (1995).
2. S.J. Sherwin and G.E. Karniadakis, 'Tetrahedral *hp* finite elements: algorithms and flow simulations', *J. Comp. Phys.*, **122**, 191 (1995).
3. M. Dubiner, 'Spectral methods on triangles and other domains', *J. Sci. Comp.*, **6**, 345 (1991).
4. I. Lomtev, C.B. Quillen, and G.E. Karniadakis, 'Spectral/*hp* methods for viscous compressible flows on unstructured 2D meshes', *J. Comp. Phys.*, **144**, 325–357 (1998).
5. B. Cockburn and C.-W. Shu, 'TVB Runge–Kutta local projection discontinuous Galerkin finite element method for conservation laws II: general framework', *Math. Comp.*, **52**, 411–435 (1989).
6. B. Cockburn, S.-Y. Lin and C.-W. Shu, 'TVB Runge–Kutta local projection discontinuous Galerkin finite element method for conservation laws III: one-dimensional systems', *J. Comp. Phys.*, **84**, 90–113 (1989).
7. B. Cockburn, S. Hou and C.-W. Shu, 'The Runge–Kutta local projection discontinuous Galerkin finite element method for conservation laws IV: the multi-dimensional case', *J. Comp. Phys.*, **54**, 545 (1990).
8. B. Cockburn and C.-W. Shu, 'P^1–*RKDG* method for two-dimensional Euler equations of gas dynamics', In *Proc. 4th Int. Symp. on CFD*, UC Davis, 1991.
9. R. Biswas, K. Devine and J. Flaherty, 'Parallel, adaptive finite element methods for conservation laws', *Appl. Numer. Math.*, **14**, 255–283, 1994.
10. B. Cockburn and C.-W. Shu, 'The local discontinuous Galerkin for time dependent convection–diffusion systems', *SIAM J. Numer. Anal.* (1998) to appear.
11. F. Bassi and S. Rebay, 'A high-order-accurate discontinuous finite element method for the numerical solution of the compressible Navier–Stokes equations', *J. Comp. Phys.*, **131**, 267 (1997).
12. F. Bassi, S. Rebay, M. Savini, G. Marioti and S. Pedinotti, 'A high-order-accurate discontinuous finite element method for inviscid and viscous turbomachinery flows, in *Proc. 2nd Europ. Conf. on Turbomachinery*, *Fluid Dynamics and Thermodynamics*, Antwerp, Belgium, March 5–7, 1997.
13. C. Johnson, *Numerical Solution of Partial Differential Equations by the Finite Element Method*, Cambridge University Press, Cambridge, 1994.
14. G. Jiang and C.W. Shu, 'On a cell entropy inequality for discontinuous Galerkin methods', *Math. Comp.*, **62**, 531 (1994).
15. A. Beskok, 'Simulations and models for gas flows in micro-geometries', *Ph.D. Thesis*, Princeton University, June, 1996.
16. M. Hammache and M. Gharib, 'An experimental study of the parallel and oblique vortex shedding from circular cylinders', *J. Fluid Mech.*, **232**, 567–590 (1991).
17. R.D. Henderson, 'Details of the drag curve near the onset of vortex shedding', *Phys. Fluids*, **7**, 1–3 (1995).
18. M.S. Bloor, 'The transition to turbulence in the wake of a circular cylinder', *J. Fluid Mech.*, **19**, 290 (1964).

19. 'Numerical simulation of compressible Navier–Stokes equations—external 2D flows around a NACA0012 airfoil', in INRIA (eds.), *GAMM Workshop*, December 4–6 1985, Nice, France, Centre de Rocquefort, de Rennes et de Sophia-Antipolis, 1986.
20. D. Gottlieb and S.A. Orszag, *Numerical Analysis of Spectral Methods*, SIAM, Philadelphia, 1977.
21. W. Cai, D. Gottlieb and C.W. Shu, 'Non-oscillatory spectral Fourier methods for shock wave calculations', *Math. Comp.*, **52**, 389–410 (1989).
22. J. Giannakouros and G.E. Karniadakis, 'A spectral element—FCT method for the compressible Euler equations', *J. Comp. Phys.*, **115**, 65 (1994).

